Pergamon

Acta mater. 49 (2001) 3647–3657

Acta MATERIALIA

www.elsevier.com/locate/actamat

HVTEM *IN SITU* OBSERVATIONS OF DISLOCATION MOTION IN THE OXIDE DISPERSION STRENGTHENED SUPERALLOY MA 754

D. HÄUSSLER[1], M. BARTSCH[2], U. MESSERSCHMIDT[2]† and B. REPPICH[1]

[1]Institut für Werkstoffwissenschaften, Lehrstuhl 1, Universität Erlangen-Nürnberg, 91058 Erlangen, Germany and [2]Max-Planck-Institut für Mikrostrukturphysik, Weinberg 2, 06120 Halle/Saale, Germany

(Received 7 May 2001; received in revised form 17 July 2001; accepted 17 July 2001)

Abstract—*In situ* straining experiments in a high-voltage transmission electron microscope have been performed on the oxide dispersion strengthened nickel-base superalloy INCONEL MA 754 at 1020 and 1065 K. The dislocations are pinned at the particles and bow out between them. After breaking free from the particles, the dislocations move in a viscous way. At low average dislocation velocities, the waiting time between full bow-out and detachment is larger than the time for the motion in-between the particles and the bowing-out, suggesting that the interfacial pinning mechanism is rate-controlling. At higher velocities, the waiting time is small compared to the time for bowing-out. Nevertheless, the particles impede dislocation motion due to the back stress which results from bowing. The spacings between the dispersoid particles along the curved dislocation segments, the curvature of the segments, the angles of attack as well as locally acting effective shear stress are estimated from the video recordings using the DeWitt–Koehler line tension model. The results are compared with earlier conventional post-mortem TEM data and macroscopic deformation data from the literature.

Keywords: Oxide dispersion strengthening; Mechanical properties; Creep; Dislocations; Mobility; Transmission electron microscopy (TEM)

1. INTRODUCTION

To improve the creep resistance of high-temperature materials, incoherent, non-shearable, hard oxide particles can be incorporated into a metallic matrix leading to the so-called oxide dispersion strengthened (ODS) materials. At low temperatures, the dispersoids have to be bypassed through the formation of Orowan loops. At high temperatures, this mechanism may also operate when the strain rate is high. At usual strain rates, however, the particles can be overcome through climb [1]. Nevertheless, they cause an improvement in the creep strength and lead to threshold stress-like behaviour [2]. This behaviour is attributed to an attractive interaction between the dislocations and the particles, called interfacial pinning first analysed by Srolovitz *et al.* [3]. In the model of Arzt and Rösler [4, 5], the rate-controlling step is the thermally activated detachment from the pinned configuration. Reppich [6] has recently refined the model of the combined climb-detachment process by considering statistical arguments if the particles act as weak obstacles. Dislocations pinned to particles have been observed by conventional post-mortem transmission electron microscopy (TEM) [7–9]. The parameters of the model have usually been determined from the size and density of particles and from the analysis of macroscopic deformation data [2, 10–15]. However, convincing evidence that the dislocations spend most of their time in the pinned configurations at the departure side of the particles, as is predicted by the model, has not been given by conventional TEM. However, *in situ* straining experiments in a high-voltage transmission electron microscope (HVTEM) allow the direct observation of moving dislocations and should therefore be suited to imaging essential details of the interaction process operating between dislocations and particles [16]. Up to now, only very few *in situ* experiments have been performed on particle strengthened materials. Yeh *et al.* [17] reported of predeformed Al 1 vol% Be in which a part of the dislocations was attracted by Be-rich particles during *in situ* heating up to 585 K in an HVTEM. A successful *in situ* experiment was also performed on a non-commercial ODS ordered intermetallic alloy [18]. Recently, for the ferritic ODS superalloy INCOLOY MA 956 Bartsch *et al.* [19] observed at intermediate temperatures that the dislocation motion is mainly

† To whom all correspondence should be addressed. Tel.: +49-3455582927; fax: +49-3455511223.

E-mail address: um@mpi-halle.de (U. Messerschmidt)

1359-6454/01/$20.00
PII: S1359-6454(01)00285-3

controlled by a viscous friction mechanism, while above about 1150 K thermally activated detachment from oxide particles may be the controlling mechanism.

The present paper reports on *in situ* straining experiments in an HVTEM on the nickel-base superalloy INCONEL MA 754† as a representative austenitic ODS system which obtains its high strength predominantly from finely dispersed hard incoherent oxide particles, which are considered to act as effective obstacles to the dislocation motion. It is technologically widely controlled, and as a material for high-temperature applications well-established. Its high-temperature deformation behaviour as well as the particle and the dislocation microstructure have already been investigated intensively [2, 10–12]. The present *in situ* straining experiments aim at:

1. presenting a direct evidence that the dislocations are indeed pinned to the particles at high temperatures and overcome them by a serial climb-detachment process;
2. yielding relevant geometric parameters of the arrangement of the dislocations in the pinned configurations; and
3. giving information on the dynamic properties of the dislocations.

The use of an HVTEM has the advantage of a transmittable specimen thickness which is considerably larger than the distance between the particles, this being the relevant microstructural parameter. Thus, the observed behaviour of individual dislocations should be representative for the bulk material. First results of the study were presented in [20].

2. EXPERIMENTAL

INCONEL MA754 is a nickelbase superalloy produced by mechanical alloying containing 20% Cr (by weight) in solid solution, 0.3% Al, 0.5% Ti, 1% Fe, 0.05% C, and 0.6% Y_2O_3 in order to improve the creep resistance. The state investigated here contains thermally stable oxide particles of the composition $Y_2Ti_2O_7$ at a volume fraction of $f = 1.1\%$, an average diameter of $d = 13.6$ nm, and a mean particle spacing in the slip plane of $L = 95$ nm [2, 11]. As a result of a recrystallization heat treatment, a coarse grained structure with very elongated grains is established for optimum creep-rupture properties. Since the specimen area investigated in the *in situ* experiments is small with respect to the grain size, the sample regions can be regarded as parts of a single crystal. Due to the cube-on-edge texture and the equal orientation of the *in situ* specimens in the sample block, the tensile axis was always close to [010] and the foil normal close to [101].

† Trademark of Inco Alloys International Ltd.

The microtensile specimens were prepared by cutting slices of about $8 \times 2 \times 0.3$ mm^3, grinding the slices down to a thickness of 0.1 mm and electrolytic jet polishing in two steps in a solution of nitric acid and alcohol at 235 K. They were fixed to the grips of the tensile stage by two tungsten pins.

The *in situ* straining experiments were performed in an HVTEM at an acceleration voltage of 1 MV in a special double-tilting straining stage, which enables temperatures up to about 1425 K and which is fully computer-controlled [21]. A video system consisting of a transmission fluorescent screen, a mirror at an angle of 45° and a lens-coupled TV camera is provided which allows frame sequences to be recorded in TV norm (50 half-frames per second), which is sometimes not quick enough to resolve fast processes.

Since the previous macroscopic deformation experiments on MA 754 were performed at temperatures between 1123 and 1373 K [2, 10–12], it was intended to perform the present *in situ* experiments in a similar temperature range. However, at such high temperatures the specimens degraded rapidly inside the HVTEM leading to a deterioration of the properties of the electrical insulators of the electron beam heating system of the straining stage. Therefore, the experiments were carried out only at 1020 and 1065 K. At these temperatures, the specimens degraded only near the edges of the perforations at a thickness lower than about 0.1 μm. No significant differences were observed between the dislocation behaviour at the two temperatures.

3. RESULTS

3.1. Slip systems

The slip plane of dislocations with $a/2\langle 110\rangle$ Burgers vectors is {111}. For the [010] tensile axis, discussed above, there are eight equivalent slip systems with orientation factors of $m = 0.41$. In Fig. 1a the slip planes occurring, marked in the elementary cell, are displayed in the projection onto the foil plane. All Burgers vectors of $\underline{a}/2\langle 110\rangle$ type may occur except $a/2[101]$ and $a/2[10\bar{1}]$, which are perpendicular to the tensile direction. Two of the slip planes are oriented edge-on.

Figure 1b shows the shape of dislocation segments bowing out under stress. This is calculated within the framework of the line tension model as described below in more detail. The size of the loops can be characterized by the length of their minor half axis y_o. Figure 1c presents the loop of Fig. 1b projected onto the (101) image plane from each of the four possible slip planes. All dislocation segments bowing out on their slip plane should therefore either be imaged edge-on or as segments of the two loops on the right side of Fig. 1c.

The micrograph in Fig. 2 was taken in the unloaded state at room temperature after an *in situ* straining experiment in the standard geometry of Fig. 1. Many

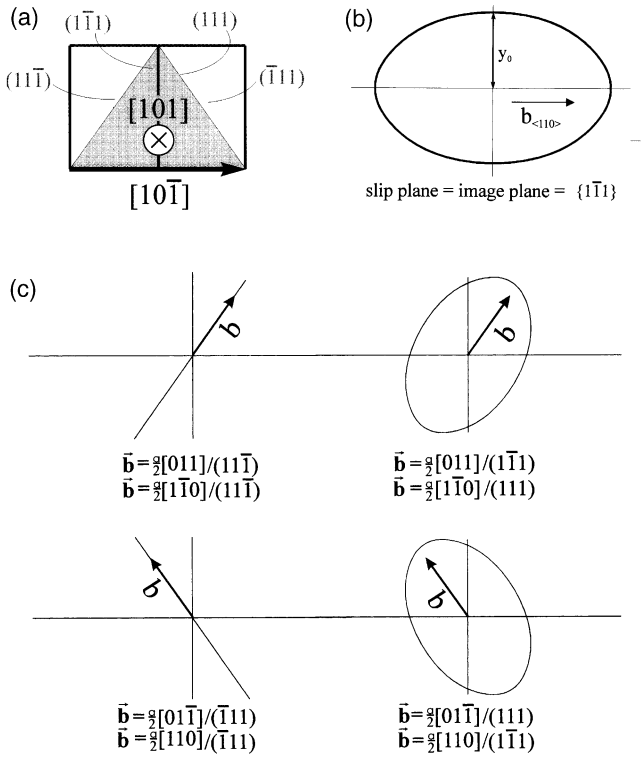

Fig. 1. (a) The four {111} slip planes in INCONEL MA 754 marked in the elementary cell for the [101] beam direction. (b) Theoretical shape of dislocation segments bowing out under stress. Burgers vector $\vec{b} = a/2\langle 110\rangle$. The image plane is equal to the {111} slip plane. (c) Projections of the theoretical shape of bowed-out dislocation segments of (b) on the (101) image plane according to a) for slip systems of non-zero orientation factors at a [010] tensile direction.

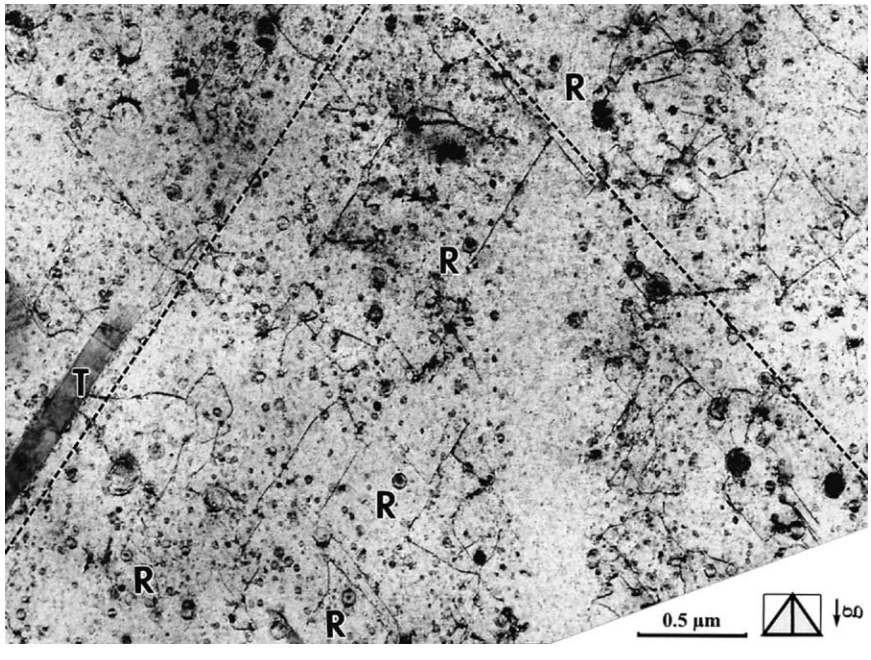

Fig. 2. Microstructure obtained after an *in situ* straining experiment at 1065 K taken in the unloaded state at room temperature. R, Loop contrasts; T, twin.

dislocations are straight indicating that they indeed lie on the slip planes that are oriented edge-on (the respective directions are indicated by broken lines). The remaining dislocations may lie on the other two slip planes. The stereo pair of Fig. 3 was taken again at room temperature in the relaxed state after an *in situ* experiment at 1020 K at an orientation tilted with respect to the standard orientation. Thus, no slip plane is oriented edge-on so that preferred orientations of the dislocation lines do not appear. A careful inspection of this figure reveals that many dislocations exhibit segments lying on different planes. This is possible by cross slip, which was observed frequently in the video recordings. Thus, in the unloaded state part of the dislocations lie on the expected {111} planes but many segments extend also on other planes.

3.2. Loop contrasts

After the *in situ* experiments, many particles are decorated by concentric rings of weak dark uniform contrast. Some of them are labelled R in Figs 2 and 3. These contrasts may belong to Orowan loops which are created around the particles by the by-passing dislocations. During the *in situ* experiments, where optimum imaging conditions cannot always be achieved, the dark contrasts around the particles became more prominent. Special contrast experiments have been performed to determine the nature of these contrasts. If they were Orowan loops, the contrast should be extinguished at the same vectors which extinguish the dislocations. Figure 5 shows two micrographs each taken with a different ⟨111⟩ type vector which should extinguish always two of the four active Burgers vectors of Fig. 1 in each micrograph. Figure 4 demonstrates that most contrast rings appear on both micrographs. Thus, the contrasts cannot unequivocally be attributed to Orowan loops of the active slip systems. Besides, the formation of Orowan loops could not directly be proved by a respective video sequence. These contrasts form also if the specimen is annealed but not deformed. Consequently, the contrast rings may appear as a result of the thermal treatment or some radiation damage during the *in situ* experiments.

3.3. Cross slip

During *in situ* experiments, cross slip can usually be easily observed from the shape of slip traces, which mark the paths of moving dislocations via deformations of surface contamination layers. Unfortunately, this artifact did not occur during the present experiments. However, changes of the motion of dislocations between inclined slip planes [(111) and $(1\bar{1}\bar{1})$ in Fig. 1b] and those imaged almost edge-on [$(\bar{1}11)$ and (111)] and vice versa have been observed a number of times. Fig. 5 presents an example. The moving dislocation is marked by arrows.

3.4. Interaction between dislocations and particles

In the following, the pinning of the moving dislocations by the dispersoids is presented by some characteristic sequences of frames taken from video recordings. Usually, the mean dislocation velocity outside the regions of the dislocation–particle interactions is typically in the range of 0.04–0.10 μm s^{-1}. The starting image of Fig. 6 shows several segments of a dislocation bowing out between particles. The forces which the dislocation exerts on the particles can be described by the angles of attack. They may

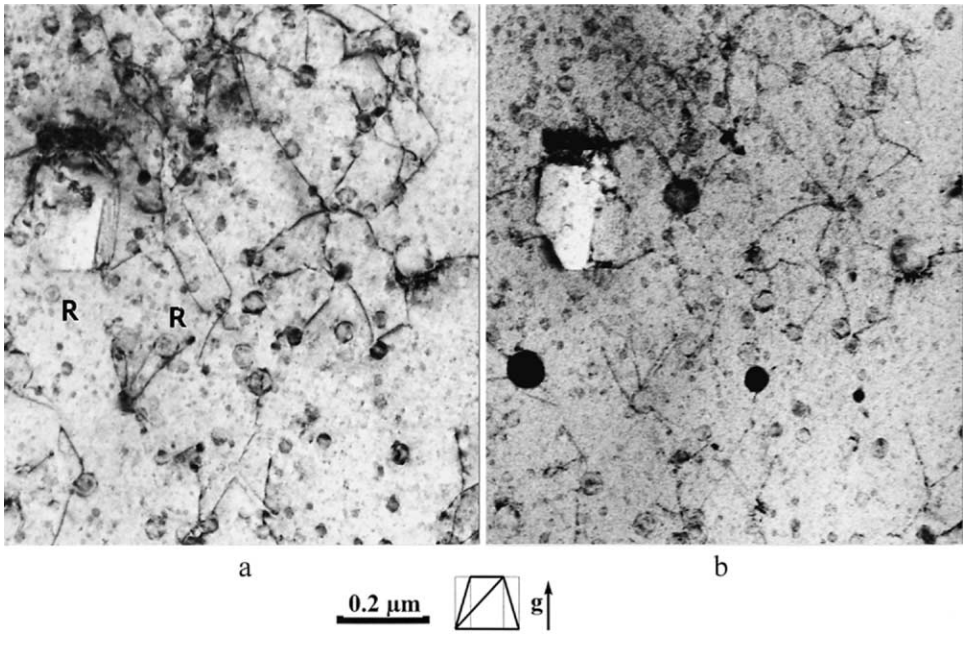

Fig. 3. Stereo pair of the microstructure obtained after an *in situ* straining experiment at 1020 K taken near the [103] pole in the unloaded state at room temperature. R, Loop contrasts.

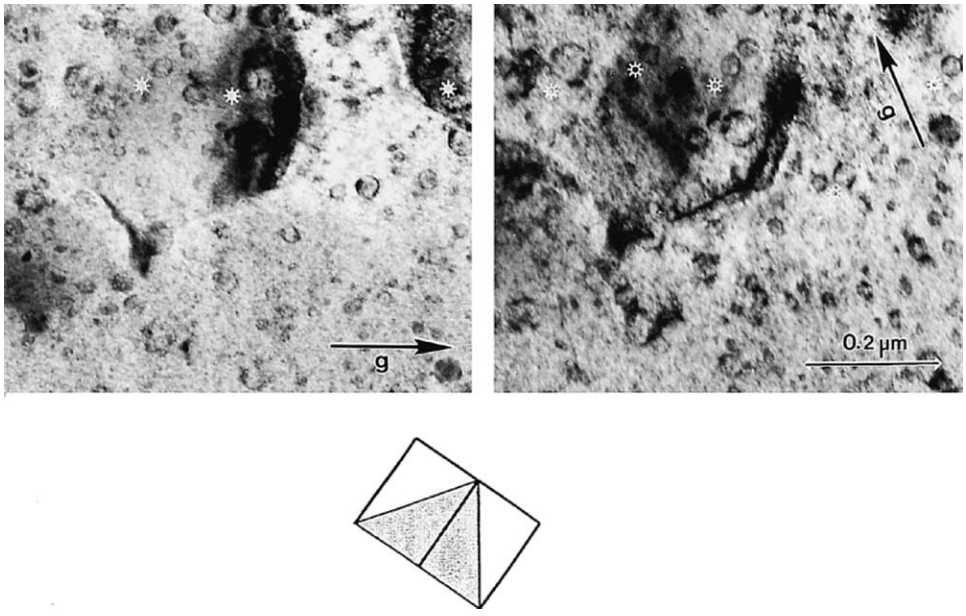

Fig. 4. Microstructure after an *in situ* straining experiment at 1020 K at different $\vec{g}$ vectors. Examples for ring-shaped contrasts marked by asterisks. (a) $\vec{g} = [11\bar{1}]$, (b) $\vec{g} = [\bar{1}11]$.

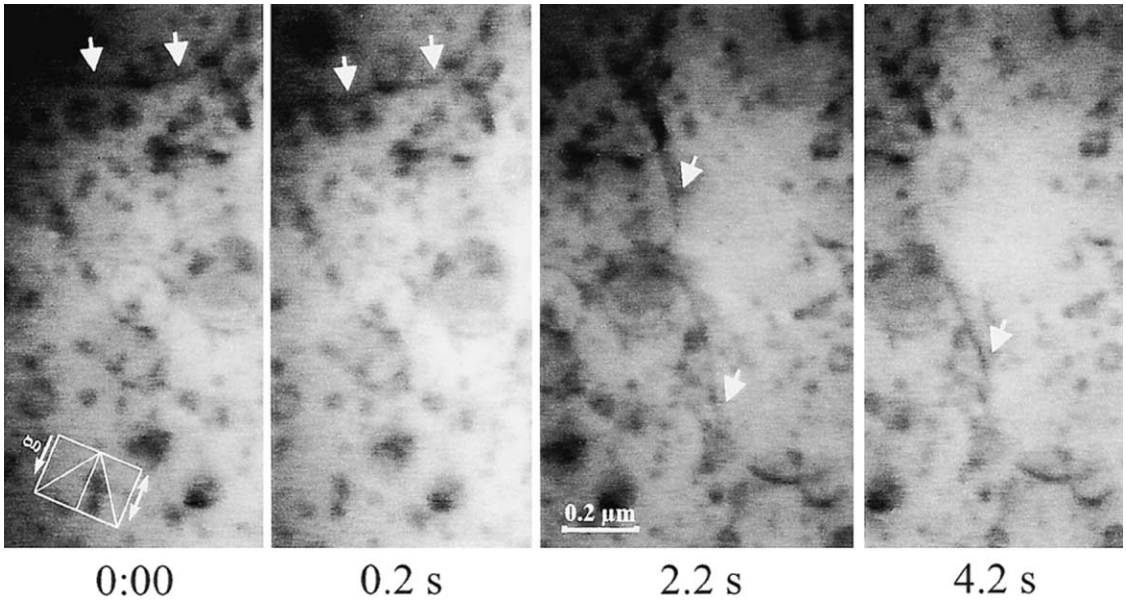

Fig. 5. Video sequence of cross slip from an inclined plane to a plane oriented almost edge-on observed at 1020 K.

be defined by the supplementary angles to 180° between the tangents of the dislocation segments contacting the obstacle, as shown in Fig. 7. The interaction forces are then given by $F = 2\Gamma\sin(\Theta/2) = 2\Gamma f$, where Γ is the line tension and $f = \sin(\Theta/2)$ a dimensionless force. In Fig. 6, the angles of attack range between about 30° and 75°. At a time of 1 s, the dislocation overcomes two obstacles, which is indicated by the double exposures in the frames at 1 and 1.1 s. Afterwards, the upper segment bows out. The final configuration is reached at 8.6 s. At 8.9 s, the dislocation has overcome the obstacle and moves quickly until it touches the next one at 9 s. It is bowed-out again at 9.2 s and has overcome the obstacle at 9.4 s. Thus, the dislocation motion appears as a sequence between pinned configurations with strongly bowed-out segments and a more or less viscous motion between the pinning points with a weaker dislocation curvature.

In Fig. 8, a dislocation approaches a particle A at

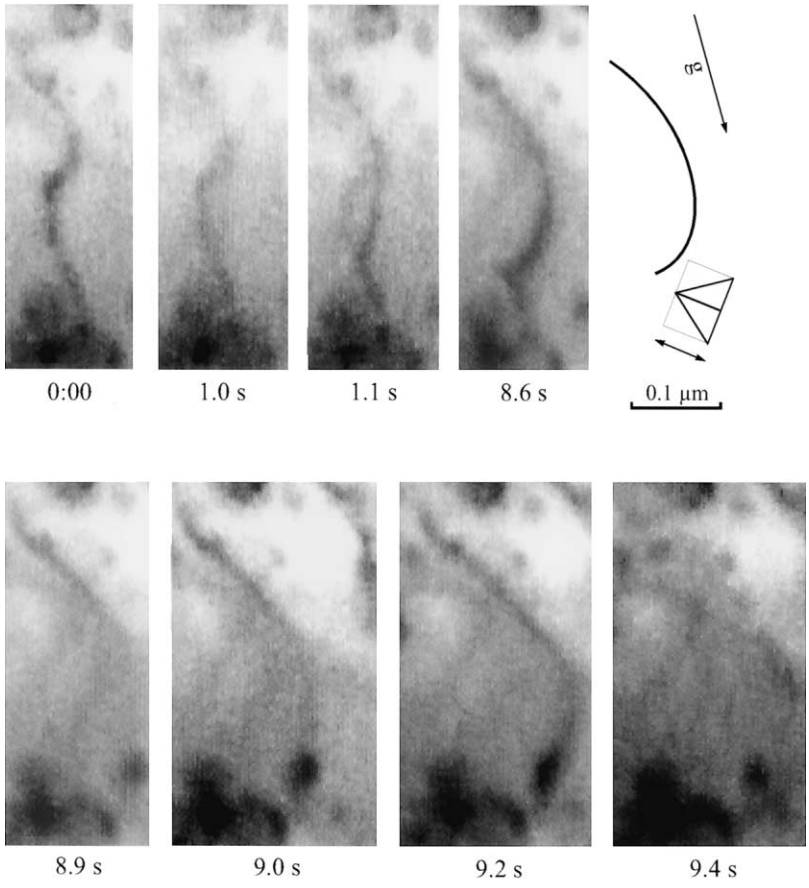

Fig. 6. Video sequence of a dislocation moving during *in situ* deformation at 1020 K. Double arrow, tensile direction. Elementary cell indicating crystallographic orientation and position of slip planes. Inclined slip plane (111) or ($1\bar{1}1$). Inset between 8.6 and 8.9 s: theoretical shape matching to the upper segment at 8.6 s.

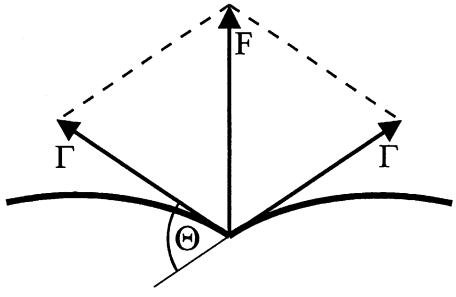

Fig. 7. Definition of the angle of attack Θ and the force F.

0 s. Its upper part continues to move until it is pinned to obstacle B and starts to bow out at 0.4 s. The bowing is completed between 0.9 and 1.2 s. After overcoming obstacle A, the upper segment moves very quickly by revolving around obstacle B. When the moving segment meets the lower segment before 1.4 s, both segments do not annihilate, which should have been possible since both segments have the same Burgers vector but opposite line directions. Instead, they form a dipole marked by the thick contrast at 2.1 s. This suggests that the large particle B has not been overcome and that the dislocation left its former slip plane by either cross-slip or climb. The angles of attack Θ at A and B at 1.2 s are about 50° and 85°. The wrapping of dispersoids has also been observed in other cases. Thus, at least very large particles are not overcome by climb but are wrapped by Orowan loops.

Figure 9 is a sequence with dislocations moving quickly at velocities exceeding 0.3 μm s^{-1}. Four dislocations are generated by a source, cross the observation area and are pinned each at the same array of dispersoids. The pinned configurations of the different dislocations reached at 0, 3, 4, and 5 s are almost identical. The dislocation segments attain their bowed-out configurations very quickly and overcome the obstacles without long waiting times. The angles of attack are between about 90° and 100°, that is, they are significantly larger than those of slowly moving dislocations, for example, in Figs 6 and 8.

3.5. Dynamic behaviour of dislocations

The dynamic behaviour of dislocations interacting with the particles is observed from the video records. It depends on the local strain rate. Two cases may be distinguished.

If the local strain rate is low, which, at least partly,

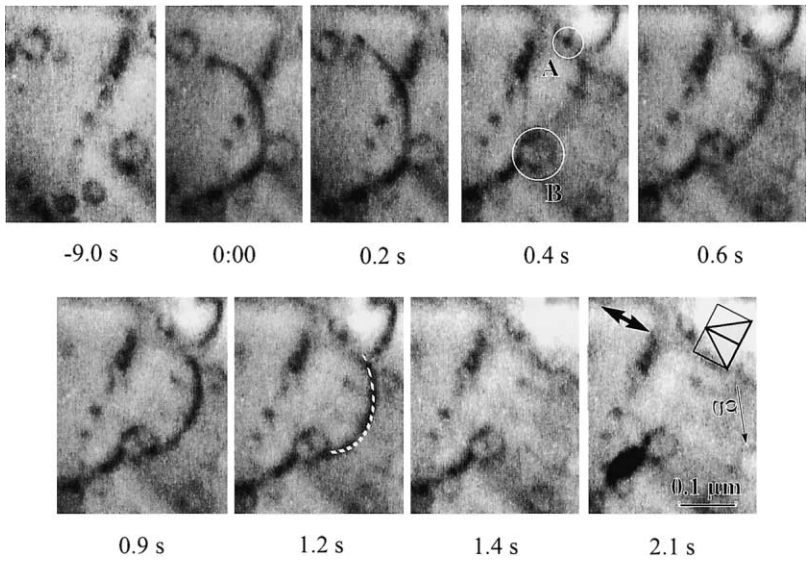

Fig. 8. Video sequence of a dislocation moving at 1020 K.

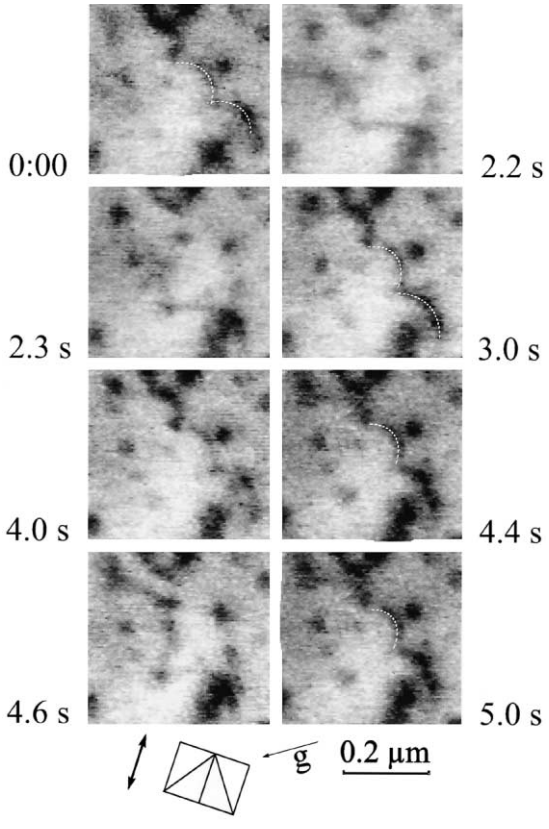

Fig. 9. Video sequence of four dislocations being pinned consecutively at the same array of oxide particles at 1020 K.

corresponds to Fig. 6, most dislocations rest at obstacles for an essential part of the total time. This is also demonstrated in Fig. 10. This series is a representative one because of the size of the observed area and the duration of the observation. However, a sequence of a few frames cannot represent all details of the dislocation movement. Relatively stable positions are attained at 0, 73, and 100.9 s in contrast to rapidly changing situations in the remaining frames of the figure. In the right column, those particles which effectively pinned the dislocations are marked by circles of a size corresponding roughly to the particle sizes. Besides, the actual and the former positions of the dislocation segments are highlighted by full and broken lines. In the second frame at 68.2 s, the contrast of the quickly moving central segment is so weak that it is almost invisible, but its position is marked in the right column. Thus, the movement of the dislocations is quite jerky on a mesoscopic scale and, considering also the comments to Figs 6 and 8, can be described in the following way. After an obstacle is overcome, the formerly pinned segment may move under the strong self stress of the backward cusp at an extremely high velocity, which frequently cannot be resolved by the video recording. Afterwards, the dislocation segment moves viscously until it touches the next particle. This finding is an indication of the Olliver and Nix effect [22], which will be discussed in more detail in Section 4. Due to the increasing self stress, which counteracts the applied stress, the dislocation segments adjoining the particle bow out slowly. At low dislocation velocities, the time for bowing is less than that for detachment from the pinned equilibrium configurations. The angles of attack range typically between about 30° and 85°, as discussed above.

Figure 9 shows that at higher local deformation rates, which are usually connected with a higher density of moving dislocations, the dislocations do not spend most of their time waiting at the obstacles. Thus, the dislocation motion is much less jerky. The times necessary for bowing out may be larger than those for detachment. Frequently, many dislocations

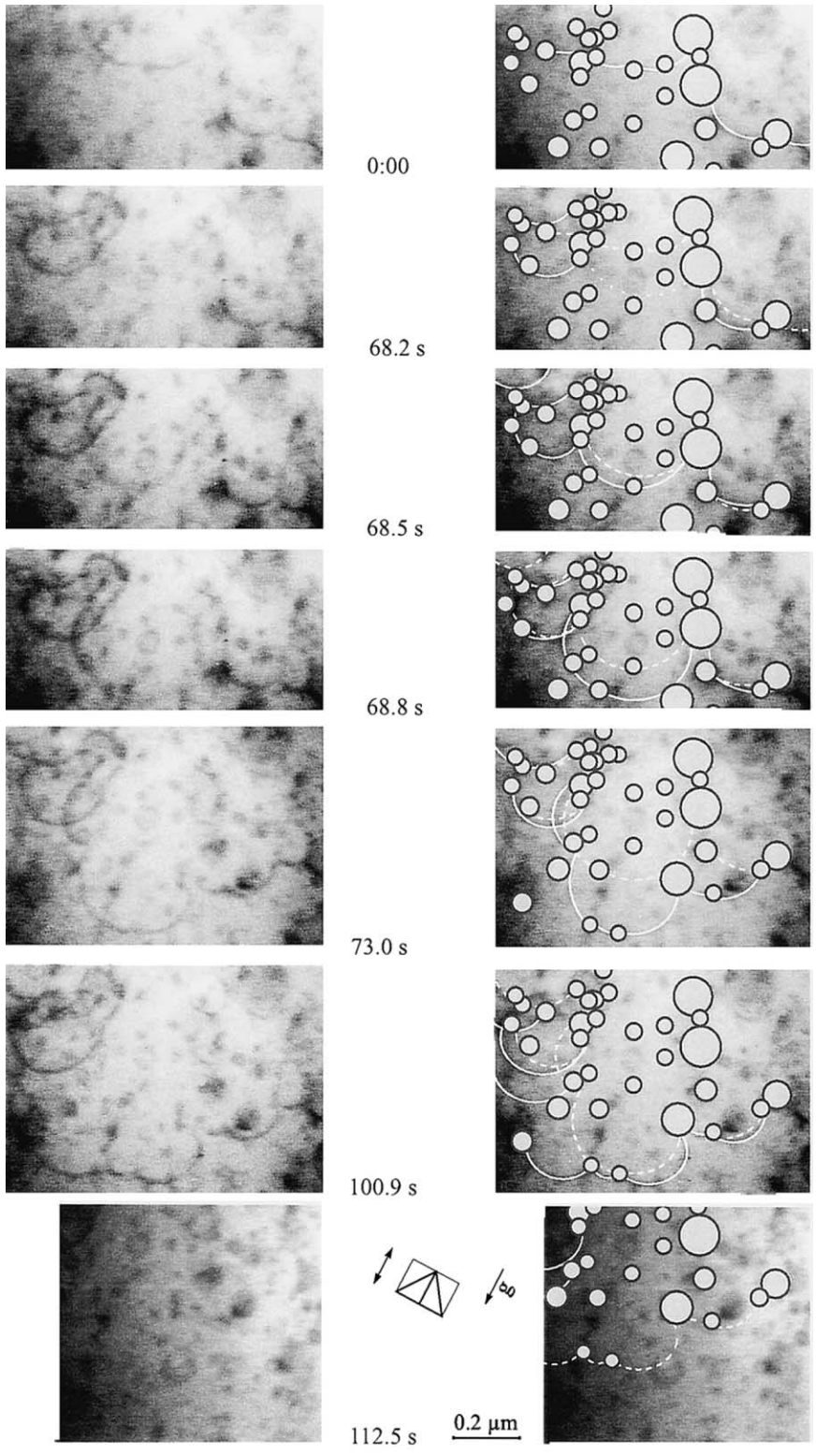

Fig. 10. Record of the movement of dislocations through an oxide particle array at 1020 K. The second to fourth frames were taken after very short time intervals. The last frame was taken immediately after the dislocation has detached from the pinned configuration. Right column, Original frames superimposed with circles labelling the positions and sizes of obstacles which effectively pinned the dislocations. Present and previous positions of dislocation segments are marked by full and broken lines.

move simultaneously. In these cases, they may move in a collective way, suggesting that long-range interactions are also important. The mean angles of attack at the obstacles are frequently >90°.

3.6. Geometric parameters of bowed-out dislocation segments

Information on the specific particle parameters can be derived from the particle spacing, *l*, that is, the average value of the distances between the particles along the dislocation lines in the pinned configurations. This can be measured directly from the video tapes as the distance between the cusps formed at the interacting dispersoids. The evaluation yields $l = 150$ nm. This value can be compared with the so-called Friedel spacing, l_F, calculated from the mean planar square lattice spacing L according to $l_F = L/(\sin(\Theta/2))^{1/2}$ (see, e.g., [1]). A proper way to estimate L consists in marking all obstacles a dislocation contacts while sweeping a certain area, as is done in Fig. 10, and dividing the swept area by the number of obstacles. The result is the area of slip plane per obstacle. The square root of this area is, evidently, equal to L. The evaluation of the micrographs yields $L = 135$ nm which is of the same order of magnitude as the earlier value $L = 95$ nm determined from the density and size of the dispersoids obtained with conventional TEM [2, 11]. The discrepancy may be due to the fact that obviously small particles either do not effectively pin the dislocations or that the weak pinning is not observed at the limited resolution of the video records. Using $L = 95$–135 nm and $\Theta = 30$–$85°$ (see above) one obtains $l_F = 110\ldots260$ nm comprising the present experimental value of $l = 150$ nm.

Bowed-out dislocation segments cause a back stress τ_b, which is superimposed on the locally acting shear stress. If the dislocation segments are in elastic equilibrium, both stresses balance each other so that the local stress can be evaluated from the curvature of the bowed-out dislocation segments, as it is reviewed in [16]. For this aim, the shape of bowed-out segments was calculated within the framework of the line tension model using elastic anisotropy [23]. Accordingly, the back stress is given by

$$\tau_b = \frac{E_s}{by_o}\ln\{1/(5b)\}, \qquad (1)$$

where E_s is the pre-logarithmic factor of the line energy of a screw dislocation, b, the absolute value of the Burgers vector, and y_o, the minor half axis of the dislocation loops, as introduced already in Fig. 1b. As the elastic constants of MA 754 were not available, the values of pure nickel, which is the main constituent of the alloy, $c_{11} = 247$ GPa, $c_{12} = 147$ GPa and $c_{44} = 125$ GPa for room temperature were used [24]. With these data and $b = 0.249$ nm there follows $E_s = 3.9\times10^{-10}$ N. The shear modulus of MA 754 of $G\cong90$ GPa at 1073 K (quoted in [11]) is slightly lower than the Voigt average shear modulus of nickel at room temperature of 95 GPa [24]. Therefore, a value of $E_s = 3.7\times10^{-10}$ N is used for the evaluations. Figure 1b presents the shape of dislocation loops in equilibrium for the $1/2\langle110\rangle$ Burgers vector on a {111} slip plane. In order to determine the characteristic size values y_o of actual bowed-out segments, loops were calculated in different sizes, projected onto the image plane of the electron micrographs as shown in Fig. 1c and printed on a transparency. This transparency was superimposed on the video prints of dislocations in stable positions, and the y_o values were read from the fitting loops. Since the Burgers vectors were not known, the loop orientation was chosen which fitted best the ellipticity of the experimental segments. Some examples are printed in Figs 6 and 8–10. Back stress data were calculated by equation (1) using the values of l and y_o measured for each segment. The average value of 16 representative segments is $\tau_b = 90$ MPa (which corresponds to $y_o = 78$ nm).

4. DISCUSSION

The present experiments give some evidence that the motion of the dislocations is not confined to single {111} planes. The dislocations cross slip frequently between these planes as demonstrated in Fig. 5. If the dislocations do not move on single planes it can be understood that they produce dipoles after passing an obstacle as in Fig. 8.

The *in situ* experiments yield convincing evidence that the dislocation motion in INCONEL MA754 is impeded by the presence of the oxide dispersoids. At low temperatures, the incoherent, non-shearable particles have to be bypassed by the Orowan process. Although during *in situ* deformation at high temperatures loop contrasts appear at many particles, it can be seen from Fig. 4 that these do not correspond to ordinary Orowan loops. On the other hand, large particles seem to be wrapped by Orowan loops, as shown in Fig. 8. The conclusion may be that, at the majority of particles, the dislocations are pinned by the interfacial pinning mechanism [3–5]. This is corroborated by the observation that at low stresses the dislocations spend an appreciable time between being fully bowed-out and detachment. Since the Orowan process is of an thermal nature, the particles should be surmounted immediately after the neighbouring dislocation segments are fully bowed-out. The result that the dislocations are pinned at most particles by interfacial pinning is in accordance with the post-mortem TEM work of Herrick *et al.* [9], who found after compression tests between room temperature and 1373 K a transition at about 1030 K from the occurrence of Orowan loops to dislocations attached to the dispersoid particles. The argumentation is accentuated by the fact that the experimentally observed local back stress $\tau_b = 90$ MPa is significantly lower than the theoretical value of the local Orowan stress τ_{OR}. According to [25]

$$\tau_{OR} = \frac{2E}{b(l-d_s)}\left\{\ln\frac{d_s(1-d_s/l)}{b} + 0.65\right\} \qquad (2)$$

where for the Orowan stress of a screw dislocation E is the energy factor of an edge dislocation and vice versa and $d_s = (\pi/4)d$. With the energy factors for screw dislocations $E_s = 3.7\times10^{-10}$ N and for edge dislocations $E_e = 5.78\times10^{-10}$ N, $l = 150$ nm and the particle diameter $d = 13.6$ nm from Section 2, the Orowan stresses of edge and screw dislocations are $\tau_{OR\,e} = 93$ MPa and $\tau_{OR\,s} = 146$ MPa, respectively.

The measured values of the obstacle spacing l and the local back stress τ_b have to be consistent with the forces F acting on the obstacles according to

$$F = \tau_b l b. \qquad (3)$$

Taking $\tau_b = 90$ MPa and $l = 150$ nm yields $F = 3.4\times10^{-9}$ N. As described in Section 3, a dimensionless force f can be calculated by $f = F/(2\Gamma)$. Using the same logarithmic factor as in equation (1), the line tension is given by $\Gamma = \kappa \ln\{l/(5b)\}$. Taking an average value of the prelogarithmic factors κ of the line tension of screw and edge dislocations, $\Gamma \cong 2.7\times10^{-9}$ N, one obtains $f \cong 0.63 = \sin(\Theta/2)$. This corresponds to an average angle of attack of about $\Theta \cong 80°$ which well agrees with the angles of attack, observed experimentally in the critical configurations.

The high values of the local back stress as well as the normalized forces exerted on the particles characterize the latter as relatively strong obstacles, even at high temperatures where the dislocations can bypass them by climb. According to the Arzt–Rösler model [4, 5] and with G being the shear modulus and k a relaxation parameter with $0 \leqslant k \leqslant 1$, the detachment stress is given in the athermal case by

$$\tau_d = \frac{Gb}{L}(1-k^2)^{1/2}, \qquad (4)$$

or the normalized detachment force by

$$f_d = (1-k^2)^{1/2}. \qquad (5)$$

The athermal detachment force, on the other hand, corresponds to the maximum force observed in the array of obstacles, that is, $f_d = \sin(\Theta_{max}/2) \cong 0.75$ with $\Theta_{max} \cong 100°$. This leads to $k_{min} \cong 0.66$.

The present values of k and τ_b reflecting the process of bypassing the particles can be correlated with those resulting from a recent comprehensive analysis of the macroscopic deformation data in terms of the modified threshold stress concept [2]. The authors determined the parameter k and the particle contribution to the creep strength (termed σ_p^*) from the difference of the measured compressive yield stress of MA754 and the particle-free matrix reference material Nimonic 75. The best fit of the model to the data (see Fig. 8a in [2]) yielded, for 1123 K, $k = 0.75$ or 0.81, depending on the details of the model used. Compared with this, the present value of $k = 0.66$ is quite low. Besides, taking the same orientation factor of 0.41 of the present loading geometry for the material in [2], it can be extracted from this reference that the particle strength amounts to $\sigma_p^* = 40\ldots50$ MPa (for strain rates between 10^{-2} and 10^{-7} s^{-1}), that is, half of the present value of the locally acting back stress τ_b of 90 MPa. This obvious discrepancy cannot be due to the slightly lower temperature in the present study alone and will be discussed in more detail elsewhere [26].

Let us now consider two further substantial flow stress components which, in contrast to the literature [5, 15], should not be ignored in the advanced quantitative description of the high-temperature strength of ODS materials [2, 10–14, 27]. The observed viscous motion of the dislocations between the interacting particles at high temperatures suggests that evidently their velocity is governed by a diffusion-controlled glide mechanism, as concluded previously from creep experiments on MA 754 [2, 10] and PM 2000 [13, 14] as well as from an *in situ* study on MA 956 [19]. It may be the microcreep mechanism due to solute atmospheres, particularly from the Cr as well as from trace elements in the alloy matrix. The viscous dragging mechanism adds a contribution to the flow stress at all conditions. Unfortunately, it cannot be estimated from the data in the present investigation. However, this flow stress component (termed σ_{eff} in [2]) has been deduced by modelling the steady-state creep data. As expected, the values obtained depend on the strain rate and vary between 15 and 40 MPa for MA 754 at 1123 K (after conversion into a shear stress) and thus amount to 17–44% of the local back stress τ_b. In this context the following aspect is of interest. As already mentioned in the comments to Figs 6 and 10 in Section 3, the dislocation segments which just have been detached from the attractive departure side of the particle, subsequently glide extremely fast before they move viscously until they touch the next dispersoids. This behaviour is caused by the back stress of the backward cusp at the former obstacle which supports the applied stress but it is also consistent with the idea of Olliver and Nix [22] who postulated that the matrix dislocation segments near the dispersoid particles loose their solid solution clouds at the moment of breakaway. This effect can lead to a dispersion-induced weakening in a certain range of strain rate and temperature, which the authors observed for ODS Al–Mg alloys and which explains the anomalous creep behaviour of MA 754 at medium creep rates [10].

The third essential contribution to the flow stress of the ODS alloy may originate from the deformation-induced dislocation microstructure†. The mutual elas-

† The long-range back stress due to subgrain boundaries as described by the "composite model" [27] can be ignored because the evolution of a subgrain structure is retarded in the ODS alloys under discussion [2, 13].

tic interactions between the dislocations lead to the collective motions observed. The athermal stress contribution can roughly be estimated from the Taylor hardening of parallel single dislocations according to

$$\tau_G = \alpha G b \rho^{1/2}, \quad (6)$$

where α is a numerical constant. In the as-received condition the dislocation density in MA 754 is 2×10^{12} m^{-2} and reaches a steady-state value after long-time creep of about 1×10^{14} m^{-2} [2]. Using $G = 90$ GPa as above and $\alpha = 0.23$ [2], we obtain, as a rough estimate, $\tau_G \leqslant 52$ MPa which, however, lies within the range of values resulting from the earlier modelling of the steady-state creep behaviour [2].

As a summary, the flow stress (or, rather, creep strength) of MA 754 at high temperatures may consist of three major components, namely the stress for thermally activated detachment from the particles, which should be equal to the local back stress, $\tau_b \cong 90$ MPa, a viscous solid solution dragging stress of about 15–40 MPa [2], and a long range contribution of the dislocation microstructure $\tau_G \leqslant 52$ MPa. For comparison, the compressive 0.2% yield (shear) stress† measured at the temperatures of the present experiments and a strain rate of 1×10^{-4} s^{-1} is 100 MPa (1065 K) and 120 MPa (1020 K), respectively [2]. Thus, the linear sum of the three stress contributions amounting to 157–182 MPa considerably exceeds the actual flow stress in the macroscopic experiments. It is likely that τ_b is overestimated. It was observed earlier on precipitation-hardened MgO and Al alloys that dislocations under stress seem to be far more flexible than it is described by the line tension theory applied [16]. On the other hand, the superposition law of the three stress components may not be linear. A pythagorean addition, which is suitable for superimposing the contributions of localized obstacles of similar strength, yields 105–111 MPa close to the measured yield stress. However, there is no theoretical reason to apply this procedure to the stress components of different nature in ODS alloys where linear superposition of the particle strength and of the matrix strength (which cannot be ignored) proved satisfactory [2]. Independent of these details, the microprocesses observed in this study can explain the macroscopic flow stress of the material.

Acknowledgements—The authors are grateful to Bernhard Kummer, Christian Dietzsch and Wolfgang Greie for technical help and Ms V. Pugslay for correcting the English manuscript. They thank the Deutsche Forschungsgemeinschaft for financial support.

† We prefer the 0.2% yield stress since it reflects the situation during *in situ* straining better than the steady-state flow stress achieved at large creep strains.

REFERENCES

1. Reppich, B., in *Materials Science and Technology*, Vol. 6, ed. H. Mughrabi. VCH Weinheim, New York, 1993, p. 311.
2. Heilmaier, H. and Reppich, B., in *Creep Behaviour of Advanced Materials for the 21st Century*, ed. R. S. Mishra, A. K. Mukherjee and K. L. Murty. The Minerals, Metals and Materials Society (TMS), 1999, p. 267.
3. Srolovitz, D. J., Luton, M. J., Petkovic-Luton, R. A., Barnett, D. M. and Nix, W. D., *Acta metall.*, 1984, **32**, 1079.
4. Arzt, E. and Rösler, J., *Acta metall.*, 1988, **36**, 1043–1053.
5. Rösler, J. and Arzt, E., *Acta metall.*, 1990, **38**, 671.
6. Reppich, B., *Acta mater.*, 1998, **46**, 61.
7. Schröder, J. H. and Arzt, E., *Scripta metall.*, 1985, **19**, 1129.
8. Nardone, V. C. and Tien, J. K., *Scripta metall.*, 1983, **17**, 467.
9. Herrick, R. S., Wertman, J. R., Petkovic-Luton, R. and Luton, M. J., *Scripta metall.*, 1988, **22**, 1879.
10. Heilmaier. M., Reppich, B., in *Proc. 5th Int. Conf. On Creep and Fracture of Engg. Mat. and Structure*, ed. B. Wilshire and R. W. Evans. The Institute of Materials, London, 1993, p. 231.
11. Heilmaier, M., PhD thesis, Erlangen 1993, Fortschr.-Ber. VDI, Series 5, Nr. 286, VDI-Verlag, Düsseldorf, 1993.
12. Heilmaier, M., Wunder, J., Böhm, U. and Reppich, B., *Computational Mat. Sci.*, 1996, **7**, 159.
13. Reppich, B., Heilmaier, H., Wunder, M., Baumeister, J. and Huber, T., in *Microstructure and Mechanical Properties of Metallic High-temperature Materials*, ed. H. Mughrabi, G. Gottstein, H. Mecking, H. Riedel and J. Tobolski. Wiley-VCH, Weinheim, 1999, p. 509.
14. Herzog, R., Schubert, F., Nickel, H. and Schuster, H., in *Microstructure and Mechanical Properties of Metallic High-temperature Materials*, ed. H. Mughrabi, G. Gottstein, H. Mecking, H. Riedel and J. Tobolski. Wiley-VCH, Weinheim, 1999, p. 495.
15. Arzt, E., *Res. Mech.*, 1991, **31**, 399.
16. Messerschmidt, U., *Z. Metallkde.*, 1993, **84**, 391.
17. Yeh, Y. -H., Nakashima, H., Kurishita, H., Goto, S. and Yoshinaga, H., *Materials Trans., JIM*, 1990, **31**, 284.
18. Behr, R., Mayer, J. and Arzt, E., *Intermetallics*, 1999, **7**, 423.
19. Bartsch, M., Wasilkowska, A., Czyrska-Filemonowicz, A. and Messerschmidt, U., *Mater. Sci. Engng*, 1999, **A272**, 152.
20. Häussler, D., Reppich, B., Bartsch, M. and Messerschmidt, U., *Mater. Sci. Engng*, 2001, **309/310**, 500.
21. Messerschmidt, U. and Bartsch, M., *Ultramicroscopy*, 1994, **56**, 163.
22. Olliver, W. C. and Nix, W. D., *Acta metall.*, 1982, **30**, 1335.
23. PC programme for calculating line tension data in anisotropic elasticity by D. Baither, now at the University of Munster.
24. Hirth, J. P. and Lothe, J., *Theory of Dislocations*. Wiley, New York, 1982, 837.
25. Scattergood, R. O. S. and Bacon, D. J., *Phil. Mag.*, 1975, **31**, 179.
26. Reppich, B., Häussler, D., Bartsch, M., Messerschmidt, U., Wasilkowska, A., in preparation.
27. Blum, W., in *Materials Science and Technology*, Vol. 6, ed. H. Mughrabi. VCH Weinheim, New York, 1993, p. 359.